



**HAL**  
open science

# Comparing Metrics for Evaluating 3D Map Quality in Natural Environments

Stéphanie Aravecchia, Marianne Clausel, Cedric Pradalier

► **To cite this version:**

Stéphanie Aravecchia, Marianne Clausel, Cedric Pradalier. Comparing Metrics for Evaluating 3D Map Quality in Natural Environments. *Robotics and Autonomous Systems*, 2024, 173, 10.1016/j.robot.2023.104617. hal-04128242v2

**HAL Id: hal-04128242**

**<https://hal.science/hal-04128242v2>**

Submitted on 8 Jan 2024

**HAL** is a multi-disciplinary open access archive for the deposit and dissemination of scientific research documents, whether they are published or not. The documents may come from teaching and research institutions in France or abroad, or from public or private research centers.

L'archive ouverte pluridisciplinaire **HAL**, est destinée au dépôt et à la diffusion de documents scientifiques de niveau recherche, publiés ou non, émanant des établissements d'enseignement et de recherche français ou étrangers, des laboratoires publics ou privés.

# Comparing Metrics for Evaluating 3D Map Quality in Natural Environments

Stéphanie Aravecchia\*      Marianne Clausel†      Cédric Pradalier\*

January 8, 2024

## Abstract

In this study, we focus on addressing the challenge of measuring the 3D-map quality in natural environments. Specifically, we consider scenarios where the map is built using a robot’s 3D-Lidar point cloud observations, with potential uncertainty in the robot localization. When considering a natural environment, such as a park or a forest, unstructured by nature, another difficulty arises: the data becomes extremely sparse. As a result, measuring the map quality becomes even more challenging. This study aims to compare the effectiveness of various metrics in measuring the 3D-map quality. Firstly, we evaluate these metrics in a controlled experimental setup, where the reconstructed map is created by progressively degrading the reference map using different degradation models. Secondly, we compare their ability to measure 3D-map quality at a local level, across various simulated environments, ranging from structured to unstructured. Finally, we conduct a qualitative comparison to demonstrate the robustness of certain metrics to noise in the robot localization. This qualitative comparison is done both in simulation and in a real world experiment. Ultimately, we synthesize the properties of these metrics and provide practical recommendations for their selection.

---

\*are with IRL2958 Georgia Tech - CNRS

†is with University of Lorraine

## 1 Introduction

The motivation behind this study arises from the difficulties faced in evaluating the 3D-map quality in natural environments. Typically, map quality evaluation aims to provide a single metric that reflects the overall map quality. Nonetheless, in the context of a robot autonomously mapping a natural environment for inspection or monitoring purposes, it becomes interesting to obtain a localized measure of map quality. Indeed, the map quality may not necessarily be homogeneous throughout a possibly large-scale environment.

This study specifically focuses on this scenario, where the robot’s 3D-lidar observations construct the map. In this case, the prevailing map representation is the 3D grid, where each voxel encodes information. Traditionally, this 3D grid encodes the occupancy likelihood for each voxel. However, in this common scenario, the conventional measures of map quality, namely surface coverage and reconstruction accuracy, may not always hold significant meaning, especially when dealing with natural environments that are not only sparse but also unstructured. We will demonstrate it in this study, by emphasizing the specific case of mapping a sparse, unstructured environment, such as a natural environment, first in simulation, and then with a real world experiment.

In the case of “unstructured” environments, distinct challenges arise compared to those encountered when mapping “structured” environments. The literature often focuses on 3D-mapping in “structured” environments like urban areas, as demonstrated by extensive research conducted on the Kitti Dataset [1].

However, when it comes to work in natural environments, such as those explored in [2], [3], [4] or [5], the differentiation between structured and unstructured, dense and sparse environments becomes more prominent due to the unique challenges involved. The 3D-map in a natural environment is both unstructured and sparse. It consists predominantly of empty space, with only a few points where the 3D-lidar actually hits an object, further complicated by the increased noise level inherent to natural environments. For instance, trees, by their very structure, are sparse because they offer only an aggregation of small surfaces to the Lidar. Although the sampling of a trunk from a Lidar could be dense, the sampling of small branches or leaves, will generally not be high enough to recover the underlying structure. Moreover, from a laser’s perspective, trees can behave as semi-transparent structures, thereby inducing errors in the measurements. The reason is that when laser-rays – light cones in practice – reach a small object, like a branch, often only a portion of the energy is reflected, causing inaccurate distance readings. Two other causes of errors in laser measurements, that are particularly abundant in large-scale natural environments, are linked to the distance to the objects and the incidence angle: the error increases with each of them [6]. Finally, the localization of the robot in the map is also a source of errors because the 3D-map is a probabilistic accumulation of all the point-clouds transformed in the localization frame. This study does not directly evaluate various mapping algorithms applied to natural environments. Instead, our main emphasis lies in addressing the challenges associated with assessing the quality of 3D maps in such environments.

In a possibly large-scale environment, which could also be both sparse and unstructured, the question arises: How can we evaluate the local map quality? Are the conventional metrics capable of delivering meaningful measurements? This study specifically centers around evaluating various 3D-reconstruction metrics, including both conventional and less conventional ones, with a specific focus on assessing their effectiveness in accurately measuring the map quality. First, we begin by selecting six relevant metrics: surface coverage, reconstruction accuracy, Av-

erage Hausdorff Distance, Cohen’s Kappa coefficient, Kullback-Leibler Divergence, and Wasserstein Distance. Then, we introduce a methodology that enables the comparison of reconstructed map to reference map at a local level. This is accomplished by extracting cuboid regions from both the reference map, called ground-truth in this work, and the reconstructed map, called reconstruction, and by assessing the map quality with the previously mentioned metrics. Later on, we propose an additional methodology to evaluate the capability of the selected metrics in measuring various degradation models, when the reconstructed map is iteratively degraded from the reference map. Finally, we empirically compare the metrics in situations where the 3D map is built from point clouds obtained from the robot’s observations, both in simulation and in a real world experiment. Ultimately, we present a comparison of the selected metrics, highlighting their properties, along with guidelines towards the choice of the metric depending on the application.

## 2 Related Work

### 2.1 Map building

Building a map consists in building a representation of the perceived environment that aligns with the intended purpose of the map. In robotics, the maps are commonly built with the primary objective of optimal navigation planning, such as [7]. However, there are cases where the purpose is to reconstruct a scene to enable its monitoring, such as [8]. When the purpose of mapping is to reconstruct a scene, the most common maps are volumetric maps, or 3D-grids, and meshes, or 3D-surface maps. Meshes are generally obtained from either a Lidar point-cloud or from the point-cloud derived from visual odometry. In a mesh, the surface is described by connected triangles. An optimization algorithm is applied on the point-cloud to build the mesh. Among the most widely used techniques, we can cite Ball-Pivoting Algorithm [9], Poisson Surface Reconstruction [10] or Delaunay triangulations [11], mainly applied to mesh a single object. Other methods tackle large-scale meshing, such as [7]

who includes texture in the mesh to improve its visual aspect, or [8] who build a semantic mesh representation of a large-scale environment with the Las Vegas Reconstruction Toolkit [12]. Recently, other methods have been presented to build meshes with deep learning techniques, such as Voxel2Mesh [13].

In this paper, we focus on the prevailing map representation for outdoor robotics: volumetric maps. Such a map is the discretization of the space into voxels, each voxel containing some information, such as its occupancy likelihood. Several methods provide means to build 3D-grids from 3D-Lidar point-clouds. For instance, Voxblox [14] builds 3D grids where the truncated signed distance field (TSDF) is stored for each voxel. Although that method is developed to produce high quality maps, it tends to struggle when the environment size increases. Other methods have been proven efficient to build large 3D-grids, such as Octomap. Even though Octomap might not be the most efficient, as shown in [15], it is still one of the most widely used methods.

Octomap [16] is a method to build and store an octree instead of a 3D-grid, saving memory and computation. The open-source ROS Octomap library <sup>1</sup> implements the complete probabilistic map building process. The map is constructed in a given map frame, and every point-cloud in the Lidar frame updates the map. For each point in the point-cloud, a ray-casting operation is performed. Between the robot and the returned point, the probability of occupancy of the leaves in the octree is decreased. The returned points are updated as occupied, their probability of occupancy is increased. A thorough update process has been implemented to be robust to noise in the Lidar’s point-cloud. Moreover, the leaves in the octree encode the likelihood of occupancy, or emptiness, only if a point has been observed. Therefore, the octree encodes the unknown volume, i.e. the volume represented by absent leaves, a feature that could be useful in different robotics applications, such as exploration. We use Octomap to build the probabilistic volumetric map denoted as “reconstruction” in this study.

It is also important to note that the quality of

<sup>1</sup><http://wiki.ros.org/Octomap>

the map is intrinsically linked to the precision of the robot localization and that solving the localization in large-scale natural environment is still challenging. Since the point-clouds are expressed in the Lidar frame (which is based on the robot’s localization), any error in the transformation from the Lidar frame to the map frame will lead to errors in the map [4]. For those reasons, in this study, we evaluate the different metrics through the scope of the localization precision with different level of noise in simulation.

## 2.2 3D-reconstruction metrics

### 2.2.1 Classic 3D reconstruction metrics in robotics

In the context of 3D-map quality assessment, whether for robotics applications or not, the task typically consists in measuring the quality of the 3D reconstruction, often by comparing two surfaces. Commonly, those are the mesh generated from the 3D-point cloud, and the ground-truth mesh. Traditional metrics in that case are based on surface distance errors. They consist in calculating, for all surface points of one surface, the distance to the closest on the other surface, and then extract some statistics. Common surface distance errors are the Hausdorff Distance, that we will detail later, the Root Mean Square Error (RMSE) or the MAE (Mean Average Error) (used respectively in [17], [18], [19] for instance).

In the context of robotics, the prevailing metrics of reconstruction quality are the surface coverage and the reconstruction accuracy. Both are derived from those surface distance errors, and applied either on the meshes or on the 3D-grids. In the latter case, two sets of points are compared. Provided we want to compute the surface coverage, we are interested on the proportion of the set of points from the ground-truth accurately reconstructed. To do so, if the distance between a ground-truth point and its closest reconstructed point is less than a registration distance, the ground-truth point is considered as reconstructed (i.e. valid). The metric is the proportion of such points ([20, 21]). Similarly, the reconstruction accuracy corresponds to the proportion of accurately reconstructed points in the set of points from

the reconstruction, that is, points whose distance to the closest ground-truth point is below a registration distance.

### 2.2.2 Other reconstruction metrics

Some metrics have been proved efficient when it comes to evaluate the quality of the semantic segmentation predicted by deep-learning models, although most of them have been used outside the field of computer vision for decades. The idea with those metrics is to evaluate at the same time the classification accuracy and the correctness of the localization. Among them, we can cite the accuracy, the precision, the recall, or even the Intersection Over Union (IoU, Jaccard Index), or the F1 score. [22] provides a thorough review and comparison of the existing segmentation metrics for 3D-medical image segmentation tasks. Building upon [22], [23] compares some of those metrics depending on the size of the regions of interest to segment. As [22], building on the fact that we are working on 3D-grids, we can consider our problem a 3D-segmentation problem. We can then consider each voxel is assigned the class “empty” or “occupied” based on its occupancy likelihood. In natural environments, the volume is mostly empty space, with sparse objects whose contours represent the occupied space. [23] shows that two metrics are particularly sensitive when it comes to measuring segmentation quality of small objects in an image: the Average Hausdorff Distance and Cohen’s Kappa coefficient.

The Hausdorff Distance (HD) is, as the other metrics seen before, a spatial distance metric, widely used to evaluate 3D-reconstruction [17, 24]. HD is a common measure of distance between two point sets, but it is sensitive to outliers. [22] proposes to use instead the Average Hausdorff Distance (*AHD*), introduced in [25]. The *AHD* averages the HD over all the points, becoming more stable and less sensitive to outliers than HD.

The other interesting metric pointed out by [23], is the Cohen’s Kappa coefficient (*KAP*). Unlike the metrics seen previously, *KAP* is not a spatial distance metric but a probabilistic metric. It was first proposed in [26]: it provides a score measuring the agree-

ment between two samples. As an advantage over other measures, *KAP* takes into account the agreement caused by chance, which makes it more robust. That is, *KAP* is in  $[-1,1]$ , where 1 corresponds to complete agreement, -1 to complete opposition, and 0 to random.

### 2.3 Comparing probabilities

Since we are building a probabilistic volumetric map with Octomap, we could take advantage of that framework to measure the quality of the map. Each voxel in the probabilistic map has a probability of occupancy between 0%, the absolute certainty that the voxel is empty, and 100%, the absolute certainty that the voxel is occupied. Leveraging the probabilities inside a 3D-grid is not a novelty, and has been explored in [20]. However, they do not propose a mean to compare the reconstructed volume to a reference one. They calculate the entropy of the voxels, which represents their distance to the unknown, thereby indicating the quantity of observation for each voxel, but not a measure of the reconstruction quality.

In this paper, we propose a methodology to compare two volumetric maps with probabilistic values. Different methods allow comparing probabilities. The most common is probably the Kullback-Leibler Divergence (*DKL*). The *DKL* [27] is a measure of how different a probability distribution is from another probability distribution. With the *DKL*, we can measure how the probability distribution of the reconstruction is different from the probability distribution of the ground-truth.

Nonetheless, since we are considering a grid of probabilistic voxels, we have access to another information: the Euclidean distance between voxels. As an example, if a point is erroneously reconstructed 5 cm away from an actual object, the reconstruction is better than if the erroneous point is 50 cm away. The *DKL* is not sensitive to this difference.

An alternative solution is then to find the Optimal Transport plan, linking one probability distribution to another one, with a cost function depending on the geometry [28]. From this Optimal Transport plan, we can calculate a distance, the Wasserstein Distance (*WD*) which is a generalization of the con-

cept of Earth Mover’s Distance (EMD). Computing the Optimal Transport Plan may be cumbersome, because it is an optimization problem that is not necessarily convex. To bypass computational issues, [29] regularizes the optimal transport problem by adding an entropic term, and solves it using a Sinkhorn’s fixed point iteration. [30] provides an open source Python library implementing several solvers for Optimal Transport problems, including [29]’s algorithm. With this regularized Wasserstein Distance, we can measure the quality of the 3D-reconstruction, comparing not only the ground-truth and reconstructed values of probabilistic maps but also taking into account the Euclidean distances in the errors.

### 3 Comparison Methodology

The objective of this study is to evaluate various 3D-reconstruction metrics with the expectation that these metrics will provide a meaningful measure of the map quality at a local level. Firstly, we present our methodology for extracting cuboid regions that enable the comparison of 3D-reconstructed map to reference map. Secondly, we describe the computation process for each considered 3D-reconstruction metric within these cuboid regions. Thirdly, we outline our methodology for evaluating the effectiveness of these metrics in measuring the map quality. This evaluation is conducted using controlled 3D-map obtained through the iterative degradation of the reference map. In this section, we call for convenience *reconstruction* the reconstructed 3D-map, and *ground-truth* the reference map. All the code is available open-source<sup>2</sup>.

#### 3.1 Cuboid region extraction

To enable the comparison of the local reconstruction and the ground-truth, we extract cuboid regions from both the reconstruction and the ground-truth. To do so, we discretize both volumes into two 3D-grids, of the same resolution  $RES$  and in the same reference

frame  $R_f$ . A local region is then a cuboid  $C$ . To compare the two local regions, we compute the metrics described in Sec. 3.2 between intersecting cuboids. Alg. 1 summarizes this section.

The ground-truth is the mesh of the scene used in simulation, the 3D-reconstruction is the full probability map constructed by Octomap from the robot’s observations.

For the ground-truth, we first slice the ground-truth mesh with horizontal planes, with a vertical space of  $res$ , our spatial resolution (with  $res < RES$ ). In each plane, we then calculate the intersection of the mesh and the plane, and we store it in a 3D matrix of voxel size  $res$ . Each voxel on the intersection is occupied and has a value of 1.0, all the remaining voxels are empty with a value of 0.0. Our ground-truth dataset,  $\mathcal{D}_{gt}$ , is then a 3D matrix of size  $(h_1, w_1, n_1)$ . Its associated volume in space, in the reference frame  $R_f$ , is the bounding-box  $B_{box_1}$ .

For the reconstruction, we first create a full probability map with Octomap in the same reference frame  $R_f$ , and with the same resolution  $res$ . From this octree, and its bounding-box in  $R_f$ , we initialize a 3D matrix as unknown space, i.e. values of 0.5, corresponding to the equal probability of the voxel to be occupied or empty. We then iterate on all the leaves in the octree. For each leaf, we set the probability of its associated voxels in the 3D matrix to the probability of the leaf (the unknown space is implicitly described in Octomap with absent leaves). We finally obtain the reconstruction dataset,  $\mathcal{D}_{rec}$ , a 3D matrix of size  $(h_2, w_2, n_2)$ , with a voxel resolution  $res$ , with its associated bounding-box,  $B_{box_2}$ , in the same reference frame,  $R_f$ .

Finally, we do the comparison in  $B_{box_1} \cap B_{box_2}$ . First, we load the intersection of both datasets in two 3D matrices,  $M_{gt}$  and  $M_{rec}$ : a voxel  $v_{gt}^{ijk}$  from  $M_{gt}$  corresponds to the same volume in  $R_f$  than  $v_{rec}^{ijk}$  from  $M_{rec}$ . Second, we go through both 3D matrices, and compare, cuboid region by cuboid region, the reconstruction and the ground truth. A cuboid region is a group of  $n \times n \times n$  voxels in each 3D matrix, and is noted  $C_{gt}$  or  $C_{rec}$ . Those cuboid regions are in fact large voxels of size  $RES = n \times res$ , in the 3D-grid  $B_{box_1} \cap B_{box_2}$ , in  $R_f$ , and each element in

<sup>2</sup><https://github.com/stephanie-aravecchia/3d-reconstruction-metrics>

$C_{rec}$  and  $C_{gt}$  stores the occupancy likelihood of its corresponding voxel of size  $n$  in  $R_f$ . Fig. 1 shows an example of a cuboid where  $n = 10$ .

### 3.2 Comparison metrics

This section explains how, for each cuboid region, we compute different metrics to indicate the map quality.

Since this method is developed with the objective to work also in natural environments with sparse objects, the reconstructed volume may contain more empty space than actual objects to reconstruct. A measure that would give information on occupied space only may not be representative of the complete volume. For this reason, we found it interesting to measure not only how well objects have been reconstructed, but also how well the empty space has been reconstructed. To do so, we first define two sets:  $\mathcal{U}_{occ}$ , the set of the cuboids regions containing at least one occupied voxel in  $C_{gt}$  and  $\mathcal{U}_{empty}$ , its complement. Then, we measure the reconstruction quality of the cuboids with a different metric in each set: one of the considered reconstruction metrics for the cuboids in  $\mathcal{U}_{occ}$ , the  $L_1$  norm for the cuboids in  $\mathcal{U}_{empty}$ . This study focuses on the evaluation of metrics in  $\mathcal{U}_{occ}$ .

Furthermore, because measuring reconstruction quality of unknown space is pointless, we consider a threshold before calculating our metrics. If all the probabilities in  $C_{rec}$  are close to the unknown ( $0.5 \pm 0.1$ ), we do not calculate the metrics, but set them to default values.

#### 3.2.1 Choice of Metrics

As discussed in Section 2.2, several metrics are available to measure map quality, whereas they are 3D-reconstruction metrics, or measure of distance between probabilities. We select six of them for evaluation, based on the criteria listed in Table 1.

#### 3.2.2 Surface Distance Metrics

The three surface distance metrics we consider here (surface coverage, reconstruction accuracy and Average Hausdorff Distance) are based on spatial dis-

tances between sets of points. To compute them, we define the following constants:

- $\hat{p}$  is an occupancy likelihood threshold,
- $d_r$  is a registration distance.

We also define the following variables:

- $\mathcal{U}_{rec}$  is the set of points  $P$  from  $C_{rec}$  whose occupancy likelihood is above  $\hat{p}$ ,
- $\mathcal{U}_{gt}$  is the set of occupied points from  $C_{gt}$ ,
- $n_{rec}$  is the number of points in  $\mathcal{U}_{rec}$ ,
- $n_{gt}$  is the number of points in  $\mathcal{U}_{gt}$ ,
- $\|PS\|$  is the Euclidean Distance between a point  $P$  from  $\mathcal{U}_{rec}$  to the closest  $S$  in  $\mathcal{U}_{gt}$ ,
- $\|SP\|$  is the Euclidean Distance between a point  $S$  from  $\mathcal{U}_{gt}$  to the closest  $P$  in  $\mathcal{U}_{rec}$ .

As an example, in Fig. 1, the points from  $\mathcal{U}_{gt}$  and  $\mathcal{U}_{rec}$  correspond respectively to the white voxels in  $C_{gt}$  and  $\hat{C}_{rec}$ .

#### 3.2.3 Surface Coverage

To compute  $COV$ , we apply the classical methodology in a 3D-grid, as [20], to our cuboids. We first compute the number of reconstructed points,  $k_{rec}$ , that is, points in  $\mathcal{U}_{gt}$  we consider correctly reconstructed, and then we compute the surface coverage,  $COV$ , the proportion of correctly reconstructed points.

$$k_{rec} = \sum_{S \in \mathcal{U}_{gt}} \mathbf{1}_B(\|SP\| \leq d_r) \quad (1)$$

where  $\mathbf{1}_B(b) = 1$  if  $b$ , 0 otherwise.

$$COV = k_{rec}/n_{gt} \quad (2)$$

#### 3.2.4 Reconstruction Accuracy

To compute  $ACC$ , we proceed similarly: we first compute the number of accurate points,  $k_{acc}$ , that is, points in  $\mathcal{U}_{rec}$  we considered valid, and then we compute the reconstruction accuracy,  $ACC$ , the proportion of valid points.

Acronym	Complete Name	Properties
<i>COV</i>	Surface Coverage	Surface distance-based score, widely used in robotics
<i>ACC</i>	Reconstruction Accuracy	Surface distance-based score, widely used in robotics
<i>AHD</i>	Average Hausdorff Distance	Surface distance, robust to small objects
<i>KAP</i>	Cohen’s Kappa coefficient	Score, robust to small objects
<i>DKL</i>	Kullback-Leibler Divergence	Widely used for distance between probabilities
<i>WD</i>	Wasserstein Distance	Distance between probabilities (Euclidean distance with the cost matrix)

Table 1: Criteria for evaluated metric selection

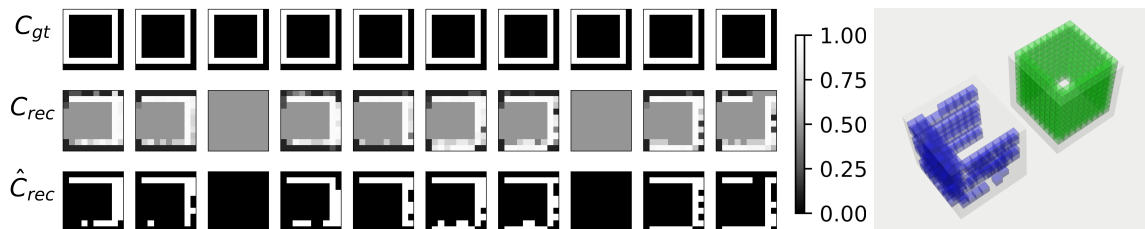


Figure 1: Visualization of a cuboid (10x10x10 voxels). On the left part of the figure, each row of images correspond to a single cuboid, each column in the row to a slice of the cuboid. The color encodes the occupancy likelihood, from free space in black, to occupied space in white, as shown in the colorbar. The grey corresponds to the unknown. The first row is the ground-truth cuboid,  $C_{gt}$ . The second row is the reconstruction cuboid,  $C_{rec}$ , encoding the occupancy likelihood. The last row is the binary version of  $C_{rec}$ :  $\hat{C}_{rec}$ , where the voxels whose occupancy likelihood is above 0.8 are set to occupied, the others to empty.  $DKL$  and  $WD_{occ}$  are computed directly  $C_{rec}$ , whereas  $COV$ ,  $ACC$ ,  $AHD$  and  $KAP$  are computed on  $\hat{C}_{rec}$ . The right part of the figure displays in green  $C_{gt}$ , in blue the thresholded  $\hat{C}_{rec}$ .

$$k_{acc} = \sum_{P \in \mathcal{U}_{rec}} \mathbf{1}_B(\|PS\| \leq d_r) \quad (3)$$

$$ACC = k_{acc}/n_{rec} \quad (4)$$

$$d_{SP} = \frac{1}{n_s} \sum_{S \in \mathcal{U}_{rec}} \|SP\| \quad (6)$$

Then, we compute the Average Hausdorff Distance, which consists in the maximum between the two distances:

$$AHD = \max(d_{PS}, d_{SP}) \quad (7)$$

### 3.2.5 Average Hausdorff Distance

To compute  $AHD$ , we follow [22]. The Hausdorff Distance measures the distance between two sets of points. We compute two Hausdorff Distances: the distance from reconstruction to ground-truth  $d_{PS}$ , and the distance from ground-truth to reconstruction  $d_{SP}$ :

$$d_{PS} = \frac{1}{n_p} \sum_{P \in \mathcal{U}_{rec}} \|PS\| \quad (5)$$

### 3.2.6 Cohen’s Kappa

The metric Cohen’s Kappa,  $KAP$ , provides a score in  $[-1, 1]$  ([worst, best]). This score provides a measure of agreement between two sets of classification. Unlike surface distance metrics seen before, we compare here directly the elements of  $C_{rec}$  and  $C_{gt}$ . In the cuboids, we consider our problem as a binary classification problem: each voxel is assigned either the class occupied or empty. In  $C_{gt}$ , each voxel already



has a value 0 (class empty) or 1 (class occupied). In  $C_{rec}$ , we consider a voxel occupied if its occupancy likelihood  $p > \hat{p}$ , else, we consider it empty and call the resulting binary cuboid  $\hat{C}_{rec}$ . Fig. 1 provides an example. We iterate on all the voxels or of  $\hat{C}_{rec}$ , compare them to their corresponding voxel in  $C_{gt}$ , and we count  $FP$  (occurrence of false positive),  $FN$  (false negative),  $TP$  (true positive),  $TN$  (true negative).

Then, to compute  $KAP$ , we follow [22]. Let  $N$  be the number of voxels in a cuboid:

$$f_c = \frac{(TN + FN)(TN + FP) + (FP + TP)(FN + TP)}{N} \quad (8)$$

$$KAP = \frac{(TP + TN) - f_c}{N - f_c} \quad (9)$$

### 3.2.7 Kullback-Leibler Divergence

The DKL provides a measure of how a probability distribution is different from a reference probability distribution. The  $DKL$  metric we use in this work is the sum of the DKL between the probability distributions derived from the elements of the cuboids. Let  $p^0$  be the occupancy likelihood of a voxel in  $C_{rec}$ ,  $g^0$  the occupancy likelihood of the same voxel in  $C_{gt}$ . For numerical reasons, we saturate  $p^0$  and  $g^0$  in  $[m, 1-m]$ , where  $m$  is a small number. The saturated values are  $p$  and  $g$ . Then, we iterate on the  $N = n \times n \times n$  elements of the cuboids, and we compute the  $DKL$  metric as follows:

$$DKL = \sum_{k=1}^{k=N} \left[ (1 - p_k) \cdot \log \left( \frac{1 - p_k}{1 - g_k} \right) + p_k \cdot \log \left( \frac{p_k}{g_k} \right) \right] \quad (10)$$

### 3.2.8 Wasserstein Distance

The Wasserstein Distance is derived from the optimal transport plan to “move” the mass distribution from a query vector to match the mass distribution of a reference vector. The cost of moving the mass being a function of the Euclidean distance it has to be moved by. Here, we calculate the Wasserstein Distance between two cuboid regions.

As this Wasserstein Distance is defined on histograms, that is, vectors that sum to 1, we first need to remap all the elements of  $C_{gt}$  and  $C_{rec}$  into two vectors of doubles,  $V_{gt}$  and  $V_{rec}$ , such that  $\forall (i, j, k) \in 0, n, V_*(i \cdot n^2 + j \cdot n + k) = C_*(i, j, k)$ . Second, we derive from each vector, two different vectors. From  $V_{gt}$ , we derive  $V_{gt}^{occ} = \max(2V_{gt} - 1, 0)$  and  $V_{gt}^{free} = \max(1 - 2V_{gt}, 0)$ . They contain respectively the probability of an element to correspond to an occupied voxel, and the probability of an element to correspond to an empty voxel. We then normalize each vector by their sum and obtain two histograms  $P_{gt}^{occ}$  and  $P_{gt}^{free}$ . Similarly, from  $V_{rec}$ , we obtain  $P_{rec}^{occ}$  and  $P_{rec}^{free}$ . We do this partition between occupancy and emptiness because we observed that the Wasserstein Distance between  $P_{rec}^{occ}$  and  $P_{gt}^{occ}$ , which embeds in each element the distance from its probability of occupancy to the unknown, contains more signal. Moreover, this corresponds better to what we intend to measure with this metric, that is how well the occupied space has been reconstructed. Using the same mapping between voxels and elements of the vector, we set the cost matrix  $M$  to contain the squared Euclidean distance between the voxels associated to the elements of the vector.

Finally, we calculate  $WD_{occ}$  the regularized Wasserstein Distance between  $P_{rec}^{occ}$  and  $P_{gt}^{occ}$ , computed using the Sinkhorn algorithm described in [29], following the implementation of [30]. This algorithm is an optimization that seeks an optimal coupling which minimizes the displacement cost of a discrete measure,  $P_{rec}^{occ}$  in our case, to a discrete measure,  $P_{gt}^{occ}$ , with respect to a cost, a transport matrix,  $M$ , under an entropic constraint. The optimal value of the optimal transport problem is the Wasserstein Distance, defined as follows, with  $\gamma \mathbf{1} = P_{rec}^{occ}$ ,  $\gamma^T \mathbf{1} = P_{gt}^{occ}$  and  $\gamma \geq 0$ :

$$WD_{occ} = \min_{\gamma} \langle \gamma, M \rangle + \alpha \cdot \Omega(\gamma) \quad (11)$$

Where  $M$  is the previously defined cost matrix,  $\Omega$  is the entropic regularization term:  $\Omega(\gamma) = \sum_{i,j} \gamma_{i,j} \log(\gamma_{i,j})$ ,  $\alpha$  is an entropic regularization factor and  $\langle \cdot, \cdot \rangle$  is the Frobenius dot-product.

In this study, we set the regularization factor  $\alpha = 1.0$ . They show in [29] that the smaller the value of

$\alpha$ , the better the precision of the algorithm, but also the slower the convergence. The value of 1 appears to be a good tradeoff, and produced satisfying results in our tests.

### 3.2.9 $L_1$ norm

In a cuboid region of the ground-truth in  $\mathcal{U}_{empty}$ , all the voxels have a probability of occupancy of 0. Therefore, when comparing the reconstruction to the ground-truth, we are comparing a vector containing some probabilities of occupancy  $V_{rec}$  to a vector of the same size containing only zeros (absolute certainty of emptiness). Such a measure is given by the  $L_1$  norm of  $V_{rec}$ : the distance between  $V_{rec}$  and the vector of zeros that represent the empty space. We do not evaluate  $L_1$  in this study, but simply provide it to the reader, because we found it convenient in other works:

$$L_1 = \sum_{(i,j,k)=(0,0,0)}^{(i,j,k)=(n,n,n)} C_{rec_{i,j,k}} \quad (12)$$

---

#### Algorithm 1 Reconstruction and ground-truth comparison

---

```

//  $\mathcal{D}_{gt}$  and  $\mathcal{D}_{rec}$  are the datasets
 $\mathcal{D}_{gt}(B_{box1}, (h_1, w_1, n_1), R_f)$ ,  $\mathcal{D}_{rec}(B_{box2}, (h_2, w_2, n_2), R_f)$ 
 $B_{box} \leftarrow B_{box1} \cap B_{box2}$ 
 $M_{gt} \leftarrow \mathcal{D}_{gt}(B_{box})$ ,  $M_{rec} \leftarrow \mathcal{D}_{rec}(B_{box})$ 
for all cuboid  $\in B_{box}$  do:
     $C_{gt} \leftarrow M_{gt}(\text{cuboid})$ ,  $C_{rec} \leftarrow M_{rec}(\text{cuboid})$ 
    if isObserved( $C_{rec}$ ) then:
        if cuboid  $\in \mathcal{U}_{occ}$  then:
            cuboid.metrics  $\leftarrow$ 
computeMetrics( $C_{rec}, C_{gt}$ )
        else:
            cuboid.metrics  $\leftarrow$  computeL1( $C_{rec}$ )
        end if
    else:
        cuboid.metrics  $\leftarrow$  maxMetrics
    end if
end for

```

---

## 3.3 Evaluation Methodology

### 3.3.1 Controlled 3D-reconstruction

This section describes the evaluation of the metrics, with a specific focus on examining their behavior in the context of decreasing reconstruction quality. We present the methodology using a single ground-truth cuboid. The key approach involves initially measuring the reconstruction quality when it is perfect, indicated by  $C_{rec} = C_{gt}$ . Then, we introduce various degradation models that are iteratively applied to the reconstructed cuboid, progressively degrading the quality of the reconstruction. This methodology is inspired from biological approaches, like [31], where the evolutionary distance between a pair of gene sequences is usually measured by the number of edit operation (substitutions, insertions and deletions) needed to transform one into the other. This distance is called the Levenshtein distance, or edit distance. Although this is not applicable here, our methodology is inspired from this concept: we apply a sequence of basic “edit” operations to increase the distance between reconstruction and ground-truth. Let us assume  $v$  is a voxel randomly sampled in the cuboid  $C_{rec}$ ,  $p(v)$  the occupancy likelihood of  $v$ , and  $v'$  a direct neighbor of  $v$ . The degradation models considered in this study are:

1.  $\mathcal{N}_{occ}$        $p(v) = 1$
2.  $\mathcal{N}_{free}$       $p(v) = 0$
3.  $\mathcal{N}_{unknown}$   $p(v) = 0.5$
4.  $\mathcal{N}_{random}$     $p(v) \sim U(0, 1)$
5.  $\mathcal{N}_{shift}$       $p(v') = p(v), p(v) = p(v')$
6.  $\mathcal{N}_{flip}$        $p(v) = 1 - p(v)$

### 3.3.2 Metric Evaluation and Comparison

$\leftarrow$  We evaluate the different metrics with a consistent perspective, focusing on their ability to discriminate reliably “good” from “less good” reconstructions. Before going further, it is important to note that some metrics are distance metrics (the lower, the better):  $DKL$ ,  $AHD$ ,  $WD_{occ}$ , whereas the others are score metrics (the higher, the better):  $COV$ ,  $ACC$ ,  $KAP$ . First, following our inspiration of distances between sequences introduced before, we define the threshold  $\hat{n}$  that divides the population of  $C_{rec}$  in two, the

“good” ones, and the “less good” ones:  $\hat{n}$  is simply a fixed level of degradation of the cuboid (i.e. 20%). Second, we define the threshold  $\hat{\theta}$  that divides the population of  $C_{rec}$  in two: the cuboids measured as “good” and those “less good”. In the case of distance metrics, a measure  $\theta$  smaller than  $\hat{\theta}$  indicates a “good” measured reconstruction (conversely for score metrics). Finally, we consider our problem as a classification problem, and we populate a confusion matrix by evaluating all the cuboids, at all the iterations as explained in Tab.2. It should be noted that the definition of true / false positive / negative described here are different from the quantities used to compute Cohen’s Kappa, where the classification was made on the voxels.

	<i>score metric</i>	<i>distance metric</i>
true positive	$(n \leq \hat{n}) \ \& \ (\theta > \hat{\theta})$	$(n \leq \hat{n}) \ \& \ (\theta \leq \hat{\theta})$
true negative	$(n > \hat{n}) \ \& \ (\theta \leq \hat{\theta})$	$(n > \hat{n}) \ \& \ (\theta > \hat{\theta})$
false positive	$(n > \hat{n}) \ \& \ (\theta > \hat{\theta})$	$(n > \hat{n}) \ \& \ (\theta \leq \hat{\theta})$
false negative	$(n \leq \hat{n}) \ \& \ (\theta \leq \hat{\theta})$	$(n \leq \hat{n}) \ \& \ (\theta > \hat{\theta})$

Table 2: Condition tested on a cuboid to populate the Confusion Matrix

From the confusion matrix, where we count the occurrence of true positive  $TP$ , true negative  $TN$ , false positive  $FP$ , and false negative  $FN$ , we compute the precision and recall of the metric:

$$precision = TP / (TP + FP) \quad (13)$$

$$recall = TP / (TP + FN) \quad (14)$$

We repeat the process for different thresholds  $\hat{\theta}$  for each metric. From this data, we are able to compare the precision recall curves for the different metrics.

## 4 Experimental Setting

This section explains how we generate the simulated worlds to conduct the metric evaluation with the controlled 3D-reconstruction (3.3.1). Then, with the same worlds, we conduct experiments, in simulation. The simulations are run within the ROS framework with Gazebo and a Clearpath Husky robot equipped with a 3D Lidar Ouster OS1-16 (16 planes of 512

points). Finally, we conduct a real world experiment, where the robot is the real version of the simulated robot, and the ground-truth of the world is acquired with a Leica Total Station.

### 4.1 World Generation

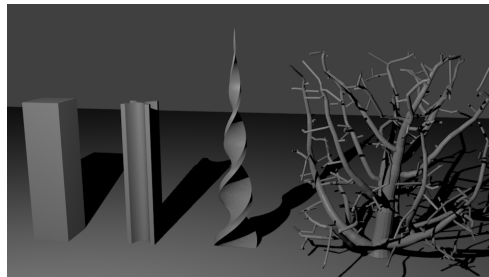


Figure 2: Illustration of the different assets used in simulation: rectangular cuboid, cross-extruded shape, helicoidal cone, simulated tree.

We generate randomly several environments. Each environment is a plane of dimension  $60m \times 60m$  on which we place assets with a Poisson Cluster Point Process, to reproduce the natural spatial distribution of trees. The assets (illustrated in Fig. 2) can be, with an increasing level of difficulty with respect to the reconstruction, either rectangular cuboids, cross-extruded shapes, helicoidal cones, or randomly selected in our 15-trees library mimicking winter bare trees or bushes. Those trees are created with a space colonization algorithm<sup>3</sup>. Due to computational considerations in Gazebo, we create only trees without leaves. Random factors are applied on the assets’ dimensions and orientation. The height of the assets ranges from 4 to 6 meters.

To a point process generation corresponds a spatial distribution that represents how the assets are arranged in the given space. From a single spatial distribution, we create four different synthetic environments, each one containing a single type of assets. With the open-source Blender software<sup>4</sup>, we create a single shapefile (.stl) for each environment. This

<sup>3</sup><https://github.com/dsforza96/tree-gen>

<sup>4</sup><https://www.blender.org/>

Point ratio	Noise formula
96%	$r = r_0 + N$ , with $N \sim \mathcal{N}(0, 0.008^2)$
3.9%	$r = r_0 - \ N\ $ , with $N \sim \mathcal{N}(0, (0.01 \times r_0)^2)$
0.1%	$r \sim U(r_{min}, r_0 + 0.03)$

Table 3: Noise mixture applied to the Lidar range

ensures that the mesh we slice to obtain the 3D-grid ground-truth is the same used in Gazebo to infer the collisions of the Lidar, hence to construct the map.

We generate 12 environments (3 distinct spatial distributions with 4 different types of asset).

From those environments, we either build 3D-reconstructions from the robot’s observations in simulation, as explained thereafter (Sec. 4.2), or we sample randomly 1500 cuboids to apply the controlled 3D-reconstruction evaluation (Sec. 3.3.1).

## 4.2 Experimental Simulation

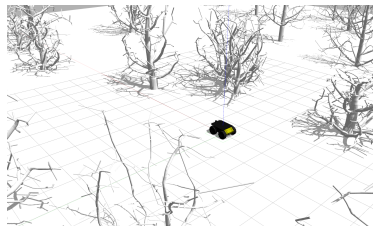


Figure 3: Illustration of an experiment in simulation.

An experiment, illustrated in Fig.3, consists in loading one of the environments described previously in Gazebo, teleporting the robot randomly in the environment, accumulating the point-cloud, and teleporting it again, for 100 iterations. Empirically, we found the mixture of noise models shown in Table 3, applied on each point-cloud, produced an output visually similar to the real point-clouds, with the same Lidar, in natural environments. For each point in the point-cloud, we compute the noisy range  $r$  as indicated in Table 3, with  $r_0$  the perfect sensor reading from Gazebo, and  $r_{min}$  the minimum range of the sensor.

Since the quality of the reconstruction is directly linked to the localization of the robot, we incrementally add noise in this localization. For each noise

level, we build a probabilistic map with Octomap. To obtain the different noise levels, we use the perfect localization from Gazebo on which we apply a Gaussian noise on the position and on the orientation. The noise levels considered in this study are (with the standard deviations  $\sigma_p$ , on position, in meter,  $\sigma_q$ , on orientation, in radian): 0. perfect localization; 1.  $\sigma_p = 0.005$ ,  $\sigma_q = 0.005$ ; 2.  $\sigma_p = 0.05$ ,  $\sigma_q = 0.01$ .

Errors in the orientation estimation lead to large errors in the position of far away points (i.e. a 0.01 radian error in the orientation leads to a 0.20m error in the position of a 20m distant point in the Lidar point-cloud). In this study, the sensor range is set to 20m, the map resolution to  $res = 0.1m$ , and the cuboid resolution to  $RES = 1m$ .

For each of the 12 environments, for each of the 3 noise levels, we run 28 simulations, for a total of 1008 experiments in simulation.

## 4.3 Experimental Setup in the field



Figure 4: Illustration of the real-world experiment. Left: the Total Station scanning the area. Right: the Husky robot driving.

The experimental site is located outside a campus and encompasses a car park area of approximately  $5400m^2$ , surrounded by a park with trees and bushes, some of which are also situated within the parking lot. Fig. 4 illustrates this experiment. Although it is not possible to acquire the ground-truth of such an environment, we consider that the 3D point-cloud obtained from its scan with a Total Station Leica TS60 is precise and dense enough to be considered as ground truth. The horizontal and vertical angular resolution of the scanning is set to 0.05 degrees. To

scan the area, the Total Station is placed on three different locations, to have different viewpoints on the trees. Each scan takes 40 to 60 minutes. At the end, we obtain a single consistent point-cloud from the area, containing  $5.5 \times 10^6$  points. The localization of the robot is provided by an RTK-GPS fused with an IMU in an Extended Kalman Filter. The position of the robot is measured in 6 different locations with the Total Station. These points are used to estimate the transformation of the RTK-GPS based frame to the Total Station frame. Because the estimate of this transform is not perfect, the error in the localization of the robot is not homogeneous. It is better in some areas of the map than in some others. We do not correct this error in this work, and use that instead to show results with different level of precision in the localization. For this experiment, the map is build with Octomap (max-range  $10m$ ), with  $res = 0.1m$ , that we compare to the ground-truth, with a cuboid resolution of  $RES = 1m$ . Because of the small vertical field of view of the Lidar, the height of the Octomap is constrained to  $6m$ . Also, to avoid large errors due to large uncertainty in the orientation, we filter out the Lidar scans associated to turning motions of the robot when we build the map with Octomap.

## 5 Results

In this section, we assess the metrics considered in this study for their capacity to offer a meaningful quality measure. We present a selection of real-world experiment cuboids, illustrating the challenge of assigning a quality score to maps, even for human observers. Thus, these examples offer insights into metric behavior, but rigorous statistical validation requires controlled maps to compare to reference maps. Consequently, the evaluation is run in simulation, where the reconstruction comes from an iterative degradation of the ground-truth, and the real-world experiments validate the evaluation.

Before delving into details, we would like to offer some preliminary information to help the understanding of this section. Firstly, Table 4 provides the acronyms used to refer to the simulated environments and the degradation models.

Acronym	Type of asset in the world
RECT	Rectangular cuboids
CROSS	Cross extruded shape
HELICOID	Helicoidal cone
TREE	Simulated tree
Degradation model	
$\mathcal{N}_{occ}$	a random voxel is set to occupied
$\mathcal{N}_{free}$	a random voxel is set to free
$\mathcal{N}_{unknown}$	a random voxel is set to unknown
$\mathcal{N}_{random}$	a random voxel is set to random
$\mathcal{N}_{shift}$	the occupancy likelihoods of two random neighbor voxels are shifted
$\mathcal{N}_{flip}$	the occupancy likelihood of a random voxel is set to its emptiness likelihood

Table 4: Summary of the acronyms used in the Results section

Secondly, Table 5 summarizes the classification of the metrics: for score metrics, higher is better, whereas for distance metrics, lower is better.

Score Metrics	Distance Metrics
Surface Coverage $COV$	Average Hausdorff Distance $AHD$
Reconstruction Accuracy $ACC$	Kullback-Leibler Divergence $DKL$
Cohen’s Kappa $KAP$	Wasserstein Distance $WD_{occ}$

Table 5: Classification of the metrics

Finally, as detailed in Sec. 3.2, surface distance metrics rely on constants, namely occupancy likelihood threshold and registration distance. For our experiments, we used common values in robotics applications (similar to [20, 21]):

- $\hat{p}$ : **0.7**, **0.8** ( $COV$ ,  $ACC$ ,  $KAP$ ,  $AHD$ ),
- $d_r$ : **0.05**, 0.1, 0.15 meters ( $COV$ ,  $ACC$ ).

For the sake of brevity, we present results only for the values in bold. Even though the metric value is slightly affected by the constants, the overall behavior remains consistent.

### 5.1 Theoretical Metrics Comparison

We compare the metrics when the reconstruction moves further from the ground-truth, following the methodology in Sec. 3.3.1, and we distinguish the experiments by type of world.

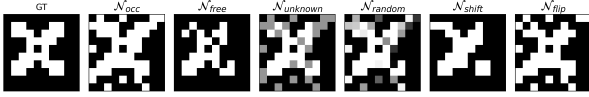


Figure 5: Visualization of the degradation models. Left-most is one slice of ground-truth cuboid. Others: degraded cuboids, after 200 iterations, with the different degradation models.

Figure 5 provides a visualization of the degradation models we are considering. The figure displays a single slice of a cuboid, from the ground-truth, and from the differently degraded cuboids, after 200 iterations.

### 5.1.1 Metrics behavior when $C_{rec}$ moves further from $C_{gt}$

We now evaluate the metrics on the 1500 sampled cuboids detailed in Sec. 4.2, with the six different degradation models. A “good” metric is expected to: be sensitive to all the types of transformations, vary monotonically when the reconstruction moves further from the ground-truth, be independent of the type of world, and give measurements in a range that does not depend too drastically on the transformations. Under this assumption, we plot for each metric, for each type of degradation, and for each type of world, how the metric behaves when the reconstruction moves further from the ground-truth. Fig. 6 shows the results in the CROSS worlds, and the complete graph is provided in Appendix . The conclusion from these graphs is that no metric satisfies all those conditions.

From each individual graph in Fig. 6 corresponding to a couple (metric, type of degradation), we can distinguish three trends, depending on how the metric vary when the reconstruction moves further from the ground-truth ( $n$  increases).

- no variation, the curve is flat: the metric is not sensitive to the type of degradation;
- a small variation (gentle slope): the metric seems slightly sensitive to the type of degradation, but we cannot conclude;
- a huge variation: the metric is sensitive to the type of degradation.

Table 6 summarizes the results of all these graphs and displays the sensitivities of the metrics to the different type of degradations.

	$\mathcal{N}_{occ}$	$\mathcal{N}_{free}$	$\mathcal{N}_{unknown}$	$\mathcal{N}_{random}$	$\mathcal{N}_{shift}$	$\mathcal{N}_{flip}$
<i>DKL</i>	✓	-	✓	✓	-	✓
<i>WD<sub>occ</sub></i>	✓	o	o	✓	o	✓
<i>COV</i>	o	✓	✓	✓	✓	✓
<i>ACC</i>	✓	o	o	✓	✓	✓
<i>AHD</i>	✓	-	-	✓	-	✓
<i>KAP</i>	✓	-	-	✓	-	✓

Table 6: Metrics apparent sensitivity to the degradation types. o: not sensitive, ✓: sensitive, -: unclusive.

Another interesting conclusion from our evaluation is that the metrics are generally dependent on the type of world. We illustrate that statement with the two graphs in the right part of Figure 6. It shows the influence of the type of world for two metrics, *ACC* and *AHD*, under  $\mathcal{N}_{occ}$  degradation model. The areas corresponding to 80% of the measures in TREES environments (red) are larger and the medians are different from the areas corresponding to 80% of RECT environments for instance (blue). That tends to indicate that not only the measure provided by the metrics are noisier in challenging environments, but also the very value supposedly dependent only on the reconstruction quality also depends highly on the type of environment. Again, the complete results are shown in Appendix .

In real world applications, the noise model is probably a combination of all the degradation models considered here, and a central question is: is there a threshold to discriminate reliably “good” and “less good” reconstructions for the chosen metric ?

### 5.1.2 Precision-Recall of the metrics

Fig. 7 shows the very challenge of setting thresholds to discriminate “good” and “less good” reconstructions, with precision-recall curves. Precision-recall curves show the tradeoff between precision and recall for different thresholds. The better the classifier, the

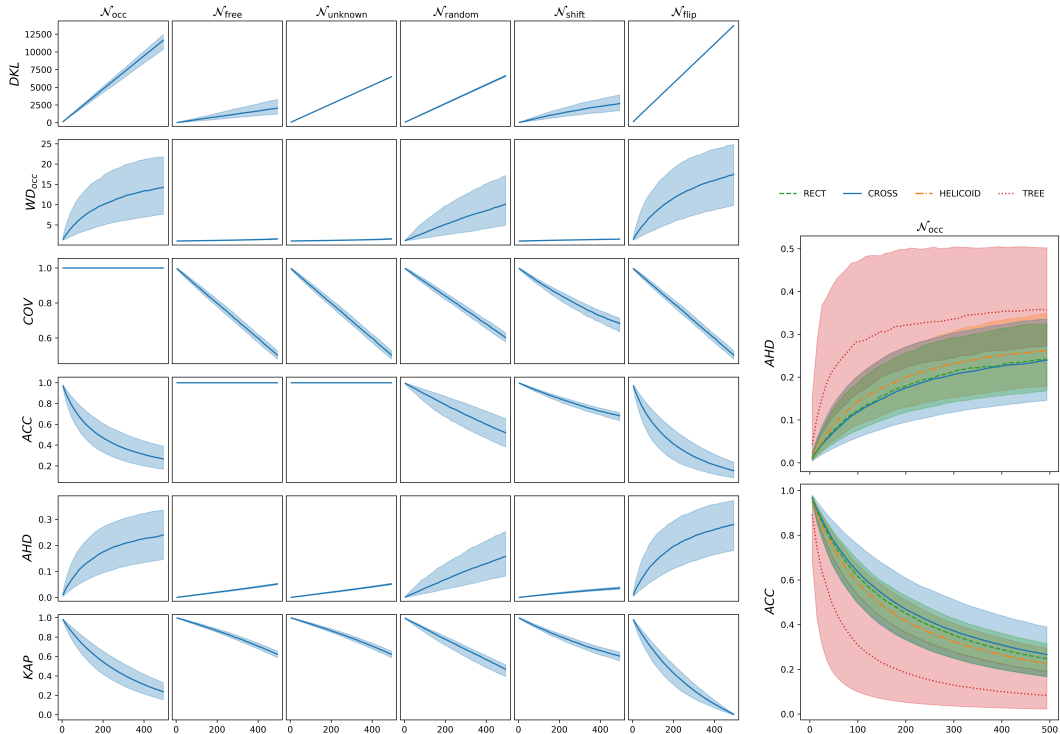


Figure 6: Left: illustration of the different metrics behavior when the reconstruction moves further from the ground-truth. One line per metric, one column per type of degradation applied to the gt. For each sub-figure, the x-axis is the number of iteration  $n$ , the y-axis the value of the metric  $\theta$ . The results are displayed only for the CROSS worlds. In each sub-figure, the line corresponds to the median value from all cuboids and the filled area shows the spread of 80% of the population. Right: Same information, displayed in all the type of worlds for  $AHD$  and  $ACC$  with a  $\mathcal{N}_{occ}$  degradation model.

closer the precision to 1 for all values of recall. This figure shows the precision-recall curves obtained as detailed in Sec. 3.3.2, where the threshold  $\hat{\theta}$  for each metric varies in a specific range. This range matches the min and max values of the y-axis of Fig.6 for the respective metric. Similarly, the distinction between “good” and “less good” reconstructions is a fixed level of degradation of the cuboids. In this evaluation, the threshold  $\hat{n}$  that divides the population of cuboids in two classes is set to 200 iterations of degradation. In other words, cuboids degraded less than 20 % are considered “good”, the others, “less good”.

For each metric, the curves are drawn with 10 val-

ues of  $\hat{\theta}$ , and we highlight three particular values with the circle, diamond and star markers. Fig. 7 displays only results in the CROSS words. The complete graph is provided in A. Fig. 7 shows that, with a specific threshold (one of the markers), a metric can perform well for certain degradation models while performing poorly for others. Finally, the two plots in the right part of the figure show that the metrics’ performance depends on the type of world: their lower performance is in the TREES worlds. Complementary to the questions marks in Table 6, these graphs suggest that  $AHD$  might be sensitive to  $\mathcal{N}_{free}$ ,  $\mathcal{N}_{unknown}$  and  $\mathcal{N}_{shift}$ , as might  $KAP$  in a slighter way. On the contrary,  $DKL$  might not be sensitive to  $\mathcal{N}_{free}$

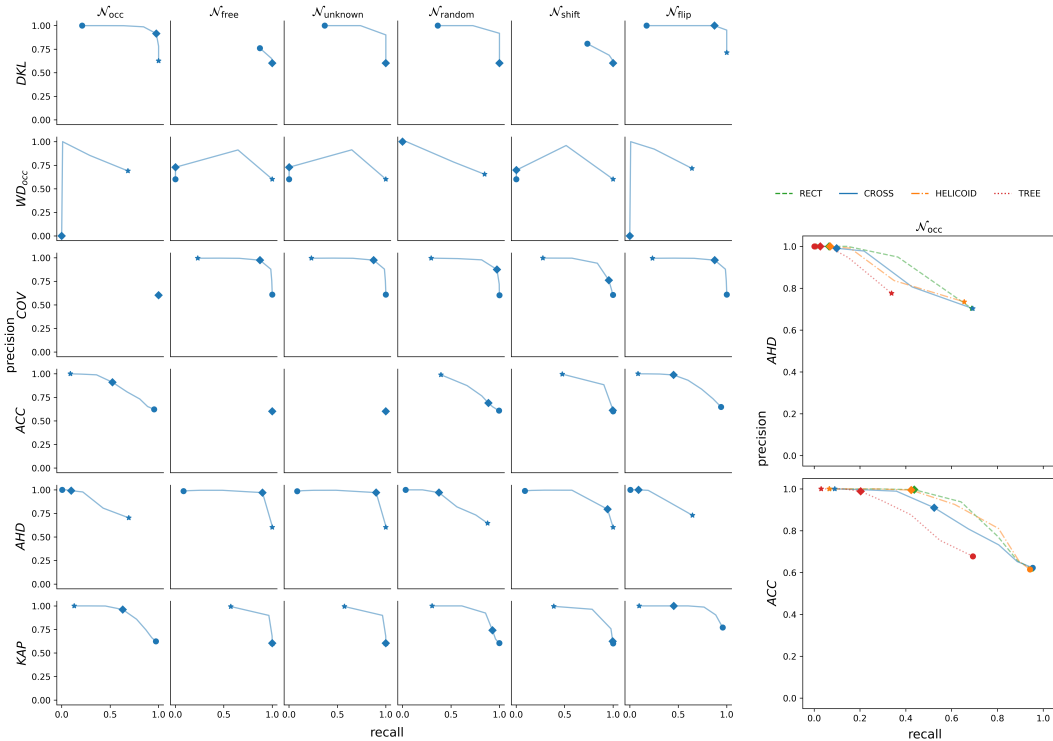


Figure 7: Left: Precision-Recall curves when we vary the value of the threshold  $\hat{\theta}$  for each metric. One line per metric, one column per type of degradation. The results are shown only for CROSS worlds. The three markers display precision-recall points for three values of  $\hat{\theta}$  for each metric. The results are displayed for a level of degradation of the cuboid of 20%. The points in (0,0) corresponds to points where it is not possible to compute precision and recall (division by 0 in Eq. 13 and 14) Right: Same information, displayed in all the type of worlds for *AHD* and *ACC* with a  $\mathcal{N}_{occ}$  degradation model.

and  $\mathcal{N}_{shift}$ .

## 5.2 Metrics Comparison on experimental reconstructions

In this section, the comparison no longer focuses on the metrics' behaviors with controlled reconstructions, but is instead directed towards their performance when the map is built from the robot's observations.

### 5.2.1 Comparison of the metrics distributions

Fig. 8 shows the distribution of the different metrics per type of world. We consider only the cuboids in  $\mathcal{U}_{occ}$ , and we display also the distribution of  $n_{gt}$  and  $n_{rec}$ , the occurrence of occupied voxels in the ground-truth and reconstruction cuboids  $C_{gt}$  and  $C_{rec}$  (Sec. 3.2).

The graphs in Fig. 8 are arranged from top to down in increasing level of difficulty in the reconstruction, from RECT (basic geometrical shape), to TREES (unstructured objects). This figure shows that determining a meaningful threshold above or be-



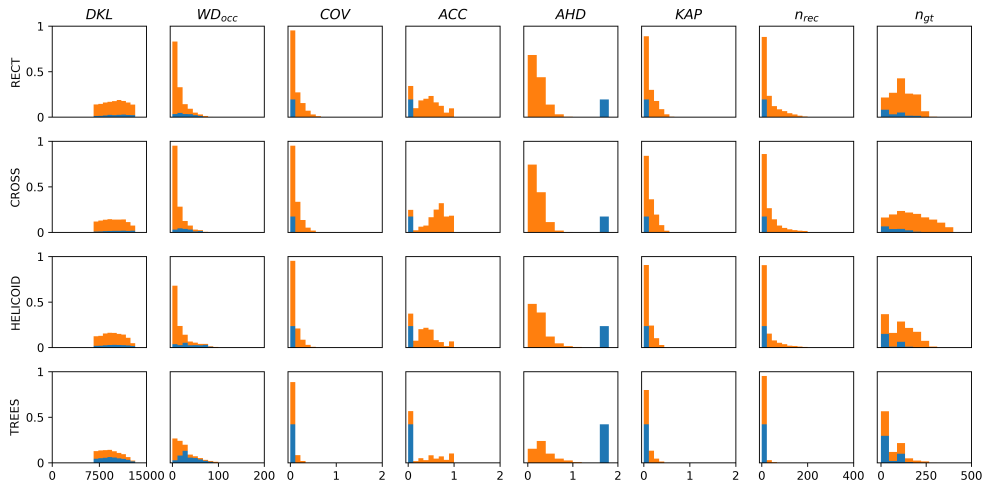


Figure 8: Distribution of the values of the metrics among the cuboids from  $\mathcal{U}_{occ}$  in the experiments. The blue corresponds to the values of the cuboids where  $n_{rec} = 0$ . The orange to the other cuboids. The values are computed only for “observed” cuboids (at least one voxel in  $C_{rec}$  has  $p < 0.4$  or  $p > 0.6$ , explained in Sec. 3.3). The figure display one line per type of world and one column per metric, with two extra-columns showing  $n_{rec}$  and  $n_{gt}$ .

low which the reconstruction can be considered good is not straightforward. This is highlighted particularly with the blue color in the histograms, corresponding to cuboids where  $n_{rec} = 0$  (denoted  $C_{rec}^0$ ). These cuboids, where not a single point have been reconstructed, are likely “bad” cuboids.

Fig. 8 shows two trends:

- The metric is likely to provide a noisy measurement: the cuboids of  $C_{rec}^0$  are spread on all the range of values.
- The range of the values the metric provides shrinks when the complexity of the world increases.

From those two trends, we can hypothesize that  $DKL$  and  $WD_{occ}$  are likely to be noisy. We can also hypothesize that  $AHD$  is the most capable of providing measures when the difficulty in the world increases: the proportion of cuboids where the value is not in the first bar is the largest. Additionally,  $AHD$  provides measures only when there is at least a reconstructed point, making it easier to identify  $C_{rec}^0$  cuboids.

Potential feature	$DKL$	$WD_{occ}$	$COV$	$ACC$	$AHD$	$KAP$
Limited noise in measurement	-	-	✓	✓	✓	✓
Robust to world complexity	✓	✓	-	-	✓	-

Table 7: Apparent advantages of the different metrics

Table 7 summarizes the apparent advantages of the metrics. We hypothesize a metric may have this potential property if it does not follow the corresponding trends described above. Table 7, Table 6 and Figure 7 all indicate that one metric seems more potent in challenging environments:  $AHD$ .

### 5.2.2 Insight on potential metrics combinations

Complementary to Table 6 on controlled reconstructions, Figure 9 shows the correlation matrix of the different metrics computed on the cuboids containing at least one reconstructed point, in all the experiments. We computed this same correlation matrix by type of

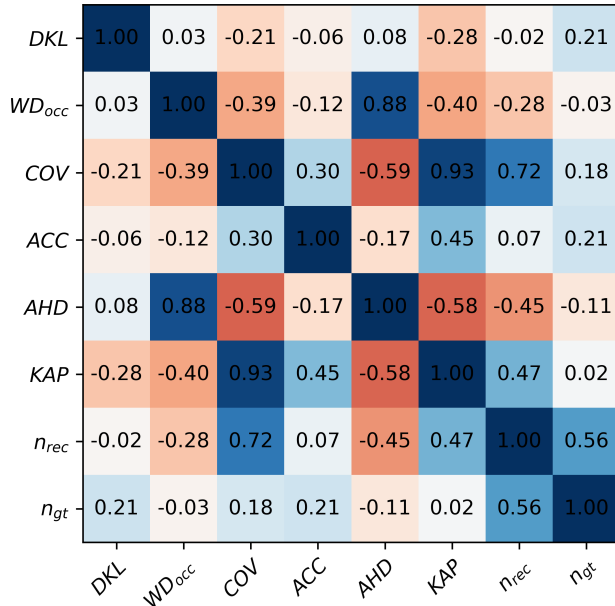


Figure 9: Correlation Matrix of the metrics. The correlation can be positive or negative depending on the type of metric (score or distance).

world, and by noise level in the localization, and although the level of correlation may change, the trend remains the same.

From that matrix, we can see that *DKL* is the metric the least correlated with the others. Our hypothesis is that *DKL* is sensitive to different information (we believe in the level of unknown in the cuboid) and may be combined with other metrics for a more reliable estimate of the reconstruction quality. Such combination is not straightforward. It would require normalizing the combined metrics in a range in which they all are meaningful, and add weighting factors. We leave that to future work.

Lastly, Table 8 presents the computation time associated with each metric. It is important to highlight that no specific optimization effort were applied to any of the implementations. Moreover, the computation of *WD<sub>occ</sub>* could greatly benefit from running on GPU. Such an implementation is provided by python-optimal-transport<sup>5</sup>. While not employed in this work

<sup>5</sup><https://pythonot.github.io/index.html>

due to its current C++ implementation and the absence of real-time inference requirements, this option holds potential. An interesting observation from this table is the efficiency of *DKL* computation, suggesting that combining it with another metric would demand a relatively small computational effort. Additionally, it’s worth mentioning that *ACC* is faster to compute than *COV* because there are generally fewer points in the reconstruction than in the ground-truth. Finally, for those interested in the computation time, *KAP* stands as promising option.

	time ( $\mu s$ )	$\pm std(\mu s)$
<i>DKL</i>	12	$\pm 1$
<i>WD<sub>occ</sub></i>	$137 \times 10^3$	$\pm 63 \times 10^3$
<i>COV</i>	230	$\pm 53$
<i>ACC</i>	11	$\pm 17$
<i>AHD</i>	241	$\pm 57$
<i>KAP</i>	5	$\pm 1$

Table 8: Comparison of the computation time

## 5.3 Qualitative comparison

### 5.3.1 Comparing reconstructions of the same cuboid

In this section, we intend to compare qualitatively the metrics on different reconstructions of the same ground-truth cuboid. To enable this comparison, we design another experiment in simulation, in a world with either a rectangular cuboid or a simulated tree. We create two sets of experiments:

- **FRONT**: the robot drives in a straight line towards the object,
- **LAT**: the robot drives in a straight line with the object on the side.

We then build the reconstructions from the robot’s observations, with different noise level in the localization (as detailed in Sec.4.2).

Fig. 10 and Fig. 11 shows the results for the same cuboid, in the **RECT** and **TREES** environments, and the three reconstructions built from the two respective driving behaviors. We focus first on Fig. 10.

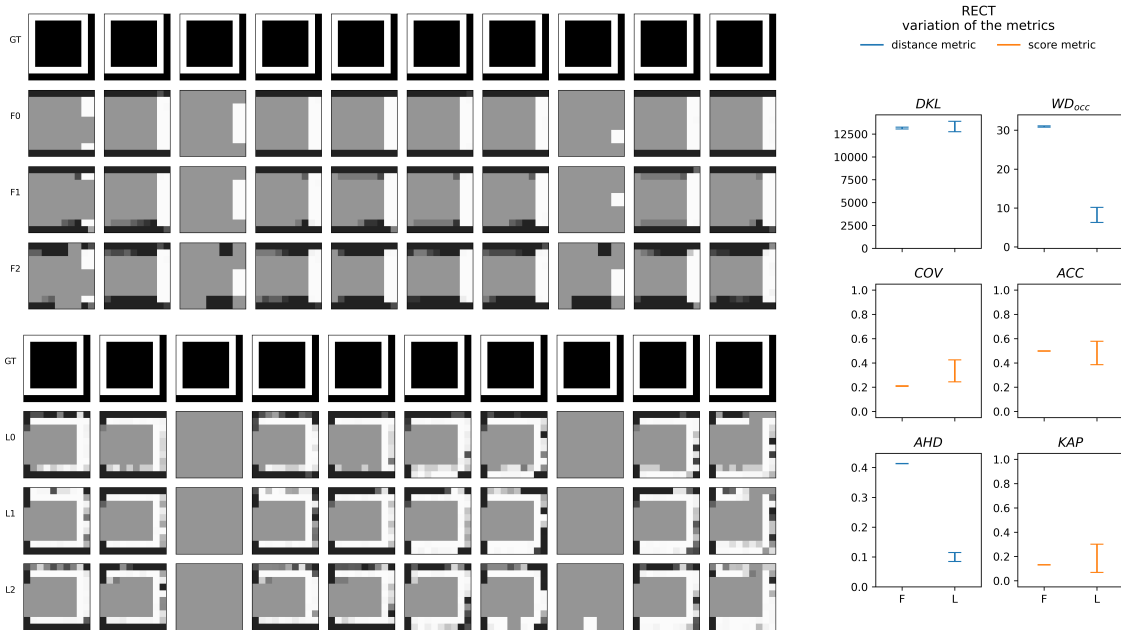


Figure 10: Example of a cuboid in a RECT environment. In the left, the first group of rows corresponds to the cuboids reconstructed with the FRONT driving behavior. GT is the ground-truth cuboid, F0, F1, F2 correspond to the reconstructions obtained with three noise level in the robot localization. The second group of rows corresponds to the LAT driving behavior. L0, L1, L2 to the reconstructions with the three noise levels. Two slices of the cuboids (3 and 8) remain mostly unknown: the Lidar used in this study is a 16-plane Lidar, and those slices remain situated between two of those planes during the experiments. The right part of the figure displays the values of the metrics, with the two different driving behaviors. Distance and score metrics are displayed with different colors to facilitate the interpretation (distance: lower is better, score: higher is better). The errorbars display the variation between the min and the max of each metric, for each driving behavior, when the reconstruction is built with the three noise levels in the robot localization.

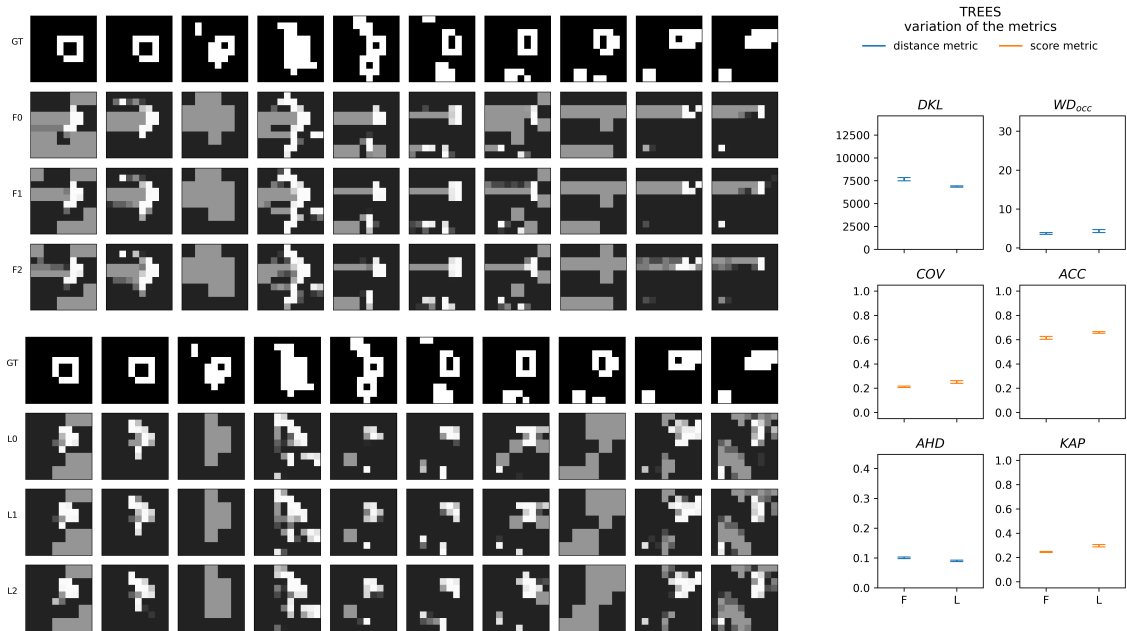


Figure 11: Example of a cuboid in a TREE environment. The figure display the same information that Fig. 10.

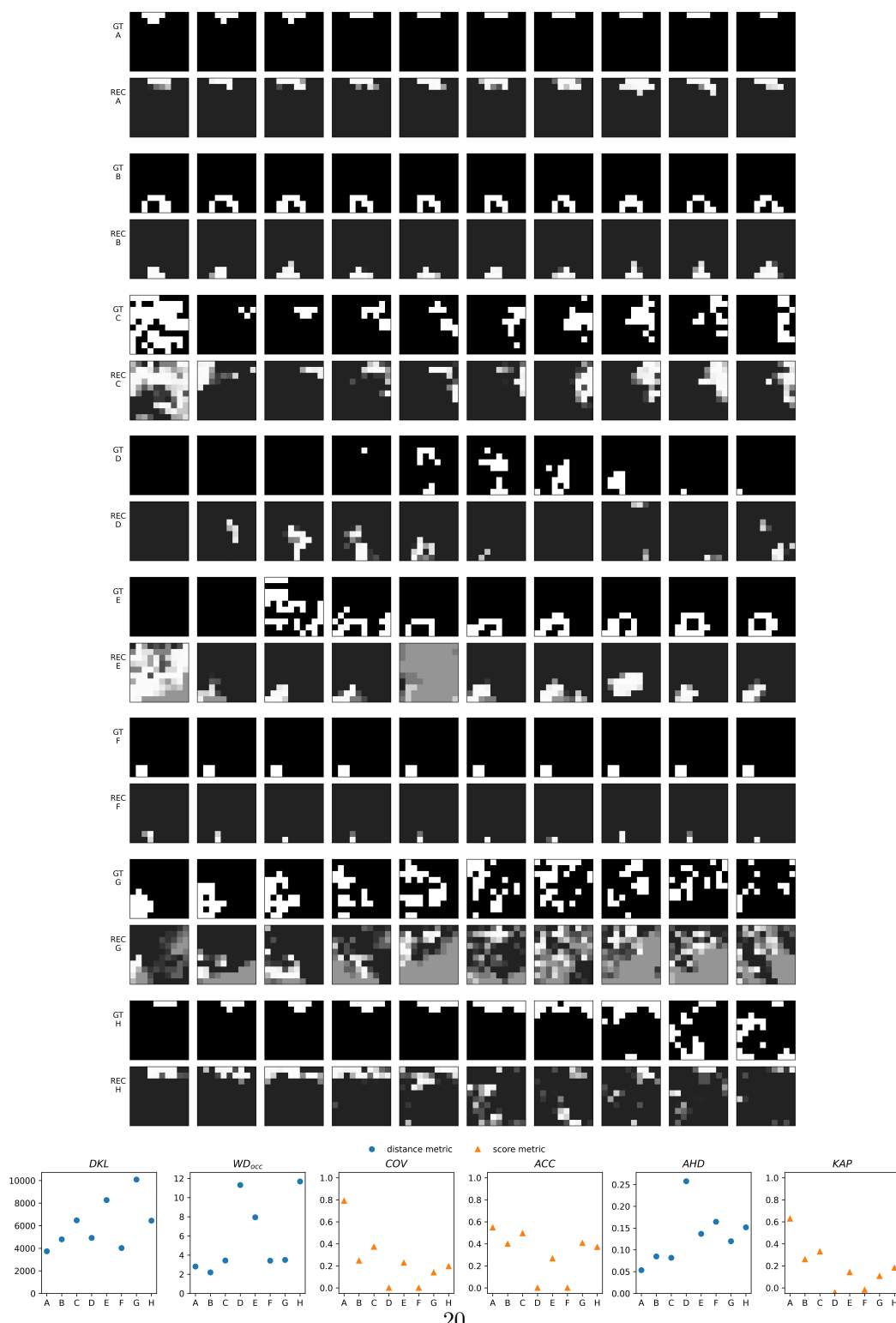


Figure 12: Example of a cuboid in a real environment. 8 cuboids are displayed (A to H). Each time, top row:  $C_{gt}$ , bottom row:  $C_{rec}$ . The last row shows the metrics corresponding to the 8 cuboids, one plot per metric. Distance metrics are blue circles, score metrics orange triangles.

In the context of an autonomous robot building a map, based on our expectations, we can presume that the maps from LAT are better than the maps from FRONT. Indeed, the group of reconstructions at the bottom of the figure appear “better” than the group at the top. We then expect the metrics to measure better reconstructions in LAT compared to FRONT. Nonetheless, the metrics yield divergent results when assessing the reconstruction quality, as they are not equally sensitive to all types of errors. For instance, *COV* measures a better reconstruction in LAT compared to FRONT, as a larger portion of the object has been reconstructed. Conversely, *ACC* measures a better map in FRONT compared to LAT, as the few points in FRONT are reconstructed more accurately. *KAP* is highly sensitive to noise in the localization: it penalizes erroneous points, regardless of the Euclidean error distance. Due to errors in the localization, discretization errors, or aliasing, an offset of one voxel, or pixel, is very likely, and a metric that penalizes such errors is very strict. We can see such errors in Fig.10. As a consequence, the variation of *KAP*’s measures in LAT includes the range of values of those in FRONT. In other words, with *KAP*, one LAT reconstruction is measured as better than the all FRONT reconstructions, whereas another one is measured as worse. On the contrary, *AHD* and *WD<sub>occ</sub>* are robust to that type of errors, as they are to noise in the localization. They provide a measure that is consistent with what one would expect in the context of autonomous robot mapping, that is, LAT are better than FRONT. *DKL* is dominated by the unknown volume of the map. It does not appear useful in this example, but it might provide information complementary to the other metrics, for instance in an exploration task, where reducing the unknown is a central feature.

Fig. 11 shows the results in the most challenging simulated environment: TREES. First, when we analyze this figure, we cannot reach an obvious conclusion, as with the previous example. Visually, the reconstructions from LAT experiments do not appear significantly better compared to FRONT experiments. However, this trend is still what is indicated by all the metrics but *WD<sub>occ</sub>*. This illustrates our claim that measuring 3D-reconstruction quality

in such an environment is a challenging task in itself.

Also, we can point out that the metrics are generally sensitive to the density of points, either in the ground-truth or in the reconstruction. When one or both is really low, we reach the limit of all those metrics.

### 5.3.2 Comparing real-world cuboids

In this section, we focus on comparing the metrics when measuring quality of real-world cuboids. We select 8 cuboids, displayed in Figure 12. Cuboids A, B and C are correctly reconstructed. The reconstruction is noisy, but we can overall recover the underlying shape of the ground-truth, in the correct location. Cuboids D, E, F, G and H are poorly reconstructed. D, E, F are reconstructed with an error in the localization: the z error (represented by the offset in the sliced images) is visible. Apart from that, we can mostly recover the underlying shape of the ground-truth in the reconstruction. G and H are also reconstructed with a z error, but are overall difficult to “grade”, because of the unstructured nature of the objects they contain (namely, branches). For a human observer, apart from assigning a better grade on cuboids A, B and C, grading all the poor reconstructions is a subjective task. The figures in the bottom of Figure 12 show how all the metrics measure these reconstructions quality. Firstly, most metrics (apart from *DKL*) generally agree that A, B, C (the first group of three symbols) are ranked in the best reconstructions. Secondly, two interesting observations emerge from the other cuboids. The first observation is that some metrics rank some poor cuboids as good as the good ones (F, G for *WD<sub>occ</sub>*, E for *COV*, G, H for *ACC*). The second observation is that some metrics do not provide any information at all on those reconstructions (D, F for *COV*, *ACC* and *KAP*). The fact that the underlying structure of the ground-truth is present, even though with an error in the localization, is completely lost in the measure. From these figures, it seems the most robust metric is *AHD*, comforting the observations from simulation. Finally, those figures also show that combining metrics, for example *AHD* and *DKL*, would likely result in a more robust metric. For instance, by doing so,

	<i>DKL</i>	$WD_{occ}$	<i>COV</i>	<i>ACC</i>	<i>AHD</i>	<i>KAP</i>
Sensitive to additional points	✓	✓	○	✓	✓	✓
Sensitive to missing points	-	○	✓	○	-	✓
Informative wrt unknown volume	✓	○	○	○	○	○
Fast to compute	✓	○	-	✓	-	✓
Proportional to Euclidean distance error	○	✓	✓	✓	✓	○
Robust to noise	-	✓	-	-	✓	○
Robust to point density	○	○	○	○	-	○
Already normalized	○	○	-	-	○	-

Table 9: Summary of the metric properties. ○: the metric does not have this property, -: it has it, but it is not a significant feature, ✓: the property is significant

the unknown remaining volume in G or E would penalize their measured distance, something *AHD* alone cannot measure.

## 5.4 Summary and Discussion

To summarize, we have seen that no metric is able to provide a meaningful measure in all the situations. Mainly, it depends on the intent of the quality measurement. Table 9 shows a summary of the metrics properties. In the context of autonomous robot mapping in natural environment, we believe a key feature is noise-robustness. When the environment is unstructured, *AHD* is probably a good choice of metric. *AHD* may be combined to *DKL* in the context of autonomous exploration, where it would also be interesting to have information on the remaining unknown volume. When the environment is structured, *ACC* or *COV* might still be good choices too, if the intent of the measure is to assess either the extent of the ground-truth surface observed (*COV*), or the precision of the reconstructed points (*ACC*), but not both at the same time. In a structured environment, their lack of robustness to point-density is counter-balanced with the underlying density of the ground-truth. Nonetheless, if the aim of the metric is to provide a robust measure of the reconstruction quality, then *AHD* remains a good choice, both in structured and unstructured environments.

## 6 Conclusion and Future Work

In this study, we have highlighted the challenges associated with assessing the 3D map quality in natural environments. We have also shown that these challenges are amplified by the unstructured nature of these environments. We have proposed a methodology for comparing the 3D-map built from the robot’s observations to the ground-truth, at a local level. While our method specifically uses Octomap’s octree, it can be adapted to other mapping techniques, as long as the produced map can be converted to a 3D-grid representation. Furthermore, we have demonstrated that the different metrics used for evaluating 3D map quality exhibit distinct properties and sensitivities to specific types of errors. Therefore, the choice of the metric should be carefully considered, based on the specific error modes we want to quantify. We have also observed that comparing the local quality of 3D map is generally feasible. However, determining an absolute threshold that reliably indicates a good reconstruction is not feasible for this set of metrics in a general case. In conclusion, our study provides practical recommendations for future research focused on evaluating the quality of 3D maps in natural environments.

Future work would follow different paths. Firstly, we could focus on combining certain metrics for a more robust map quality estimation, such as the Average Hausdorff Distance and the Kullback-Leibler Divergence. Secondly, complementary investigation could be done on the Wasserstein Distance. This

work focuses on conventional optimal transport, yet we would like to explore unbalanced optimal transport [32]. This would enable measures between positive values that are not necessary probability distributions. That would eliminate the current normalization step, allowing the comparison of cuboids with different mass. This could lead to a more robust map quality assessment. Such work would of course require GPU-based optimization implementations. Lastly, we could build upon the conclusions of this work to perform a comparative evaluation of different reconstruction algorithms.

## References

- [1] A. Geiger, P. Lenz, C. Stiller, R. Urtasun, Vision meets robotics: The KITTI dataset, *International Journal of Robotics Research* 32 (11) (2013) 1231–1237. doi:10.1177/0278364913491297.
- [2] F. Pomerleau, F. Colas, R. Siegwart, S. Magnat, Comparing ICP variants on real-world data sets, *Autonomous Robots* 34 (3) (2013) 133–148. doi:10.1007/s10514-013-9327-2.
- [3] P. F. Alcantarilla, C. Beall, F. Dellaert, Large-Scale Dense 3D Reconstruction from Stereo Imagery, 2013 IEEE/RSJ International Conference on Intelligent Robots and Systems (2013).
- [4] G. Chahine, M. Vaidis, F. Pomerleau, C. Pradalier, Mapping in unstructured natural environment: a sensor fusion framework for wearable sensor suites, *SN Applied Sciences* 3 (5) (2021) 1–14. doi:10.1007/s42452-021-04555-y.  
URL <https://doi.org/10.1007/s42452-021-04555-y>
- [5] P. Babin, P. Dandurand, V. Kubelka, P. Giguère, F. Pomerleau, Large-Scale 3D Mapping of Subarctic Forests, *Springer Proceedings in Advanced Robotics* 16 (2021) 261–275. arXiv:1904.07814, doi:10.1007/978-981-15-9460-1\_19.
- [6] J. Laconte, S. P. Deschênes, M. Labussière, F. Pomerleau, Lidar measurement bias estimation via return waveform modelling in a context of 3D mapping, *Proceedings - IEEE International Conference on Robotics and Automation 2019-May* (2019) 8100–8106. arXiv:1810.01619, doi:10.1109/ICRA.2019.8793671.
- [7] I. Ben Salah, S. Kramm, C. Demonceaux, P. Vasseur, Summarizing large scale 3D mesh for urban navigation, *Robotics and Autonomous Systems* 152 (2022) 104037. doi:10.1016/j.robot.2022.104037.  
URL <https://doi.org/10.1016/j.robot.2022.104037>
- [8] G. Chahine, C. Pradalier, G. Chahine, C. Pradalier, S.-a. Alignment, N. Outdoor, Semantic-aware spatio-temporal Alignment of Natural Outdoor Surveys To cite this version : HAL Id : hal-03738518 Semantic-aware spatio-temporal Alignment of Natural Outdoor Surveys (2022).
- [9] F. Bernardini, J. Mittleman, H. Rushmeier, C. Silva, G. Taubin, The ball-pivoting algorithm for surface reconstruction, *IEEE Transactions on Visualization and Computer Graphics* 5 (4) (1999) 349–359. doi:10.1109/2945.817351.
- [10] M. Kazhdan, M. Bolitho, H. Hoppe, Poisson surface reconstruction, in: *Eurographics symposium on Geometry processing*, Vol. 7, 2006.
- [11] S. W. Cheng, T. K. Dey, J. R. Shewchuk, Delaunay mesh generation, *Delaunay Mesh Generation* (2012) 1–386doi:10.1201/b12987.
- [12] T. Wiemann, F. Igelbrink, S. Pütz, J. Hertzberg, A File Structure and Reference Data Set for High Resolution Hyperspectral 3D Point Clouds, *IFAC-PapersOnLine* 52 (8) (2019) 93–98. doi:10.1016/j.ifacol.2019.08.101.
- [13] U. Wickramasinghe, E. Remelli, G. Knott, P. Fua, Voxel2Mesh: 3D Mesh Model Generation from Volumetric Data, *Lecture Notes in Computer Science* (including subseries Lecture



- Notes in Artificial Intelligence and Lecture Notes in Bioinformatics) 12264 LNCS (2020) 299–308. arXiv:1912.03681, doi:10.1007/978-3-030-59719-1\_30.
- [14] H. Oleynikova, Z. Taylor, M. Fehr, R. Siegwart, J. Nieto, Voxblox: Incremental 3D Euclidean Signed Distance Fields for on-board MAV planning, IEEE International Conference on Intelligent Robots and Systems 2017-September (2017) 1366–1373. arXiv:1611.03631, doi:10.1109/IROS.2017.8202315.
- [15] A. Khoche, M. K. Wozniak, D. Duberg, P. Jensfelt, Semantic 3D Grid Maps for Autonomous Driving, IEEE Conference on Intelligent Transportation Systems, Proceedings, ITSC 2022-October (2022) 2681–2688. arXiv:2211.01700, doi:10.1109/ITSC55140.2022.9922537.
- [16] A. Hornung, K. M. Wurm, M. Bennewitz, C. Stachniss, W. Burgard, OctoMap: An efficient probabilistic 3D mapping framework based on octrees, Autonomous Robots 34 (3) (2013) 189–206. doi:10.1007/s10514-012-9321-0.
- [17] N. Aspert, D. Santa-Cruz, T. Ebrahimi, MESH: Measuring errors between surfaces using the Hausdorff distance, in: Proceedings - 2002 IEEE International Conference on Multimedia and Expo, ICME 2002, Vol. 1, 2002. doi:10.1109/ICME.2002.1035879.
- [18] J. Zhou, X. Fu, L. Schumacher, J. Zhou, Evaluating geometric measurement accuracy based on 3d reconstruction of automated imagery in a greenhouse, Sensors (Switzerland) 18 (7) (2018) 1–16. doi:10.3390/s18072270.
- [19] H. Zhu, J. J. Chung, N. R. J. Lawrance, R. Siegwart, J. Alonso-Mora, Online Informative Path Planning for Active Information Gathering of a 3D Surface, in: IEEE International Conference on Robotics and Automation, 2021. arXiv:2103.09556. URL <http://arxiv.org/abs/2103.09556>
- [20] S. Isler, R. Sabzevari, J. Delmerico, D. Scaramuzza, An information gain formulation for active volumetric 3D reconstruction, Proceedings - IEEE International Conference on Robotics and Automation 2016-June (2016) 3477–3484. doi:10.1109/ICRA.2016.7487527.
- [21] S. Song, S. Jo, Surface-Based Exploration for Autonomous 3D Modeling, Proceedings - IEEE International Conference on Robotics and Automation (2018) 4319–4326doi:10.1109/ICRA.2018.8460862.
- [22] A. A. Taha, A. Hanbury, Metrics for evaluating 3D medical image segmentation: Analysis, selection, and tool, BMC Medical Imaging 15 (1) (2015). doi:10.1186/s12880-015-0068-x. URL <http://dx.doi.org/10.1186/s12880-015-0068-x>
- [23] D. Müller, I. Soto-Rey, F. Kramer, Towards a guideline for evaluation metrics in medical image segmentation, BMC Research Notes 15 (1) (2022) 1–7. arXiv:2202.05273, doi:10.1186/s13104-022-06096-y.
- [24] A. Bulbul, T. Capin, G. Lavoue, M. Preda, Assessing visual quality of 3-D polygonal models, IEEE Signal Processing Magazine 28 (6) (2011) 80–90. doi:10.1109/MSP.2011.942466.
- [25] W. J. Rucklidge, Efficiently Locating Objects Using the Hausdorff Distance, International Journal of Computer Vision 24 (3) (1997) 251–270. doi:10.1023/A:1007975324482.
- [26] J. Cohen, A Coefficient of Agreement for Nominal Scales, Educational and Psychological Measurement 20 (1) (1960) 37–46. doi:10.1177/001316446002000104.
- [27] S. Kullback, R. A. Leibler, On Information and Sufficiency, The Annals of Mathematical Statistics 22 (1) (1951). doi:10.1214/aoms/1177729694.
- [28] C. Villani, Optimal transport: old and new, Springer Verlag., 2009.

- [29] M. Cuturi, Sinkhorn distances: Lightspeed computation of optimal transport, *Advances in Neural Information Processing Systems* (2013) 1–9.
- [30] R. Flamary, N. Courty, A. Gramfort, M. Z. Alaya, A. Boisbunon, S. Chambon, L. Chapel, A. Corenflos, K. Fatras, N. Fournier, L. Gautheron, N. T. Gayraud, H. Janati, A. Rakotomamonjy, I. Redko, A. Rolet, A. Schutz, V. Seguy, D. J. Sutherland, R. Tavenard, A. Tong, T. Vayer, POT python optimal transport library, *Journal of Machine Learning Research* 22(78) (2021) 1–8.  
URL `github:https://github.com/rflamary/POT`
- [31] B. Berger, M. S. Waterman, Y. W. Yu, Levenshtein Distance, Sequence Comparison and Biological Database Search, *IEEE Transactions on Information Theory* 67 (6) (2021) 3287–3294. doi:10.1109/TIT.2020.2996543.
- [32] L. Chizat, G. Peyré, B. Schmitzer, F.-X. Vialard, Unbalanced optimal transport: Dynamic and kantorovich formulations, *Journal of Functional Analysis* 274 (11) (2018) 3090–3123.

## **A Theoretical Metrics Comparison**

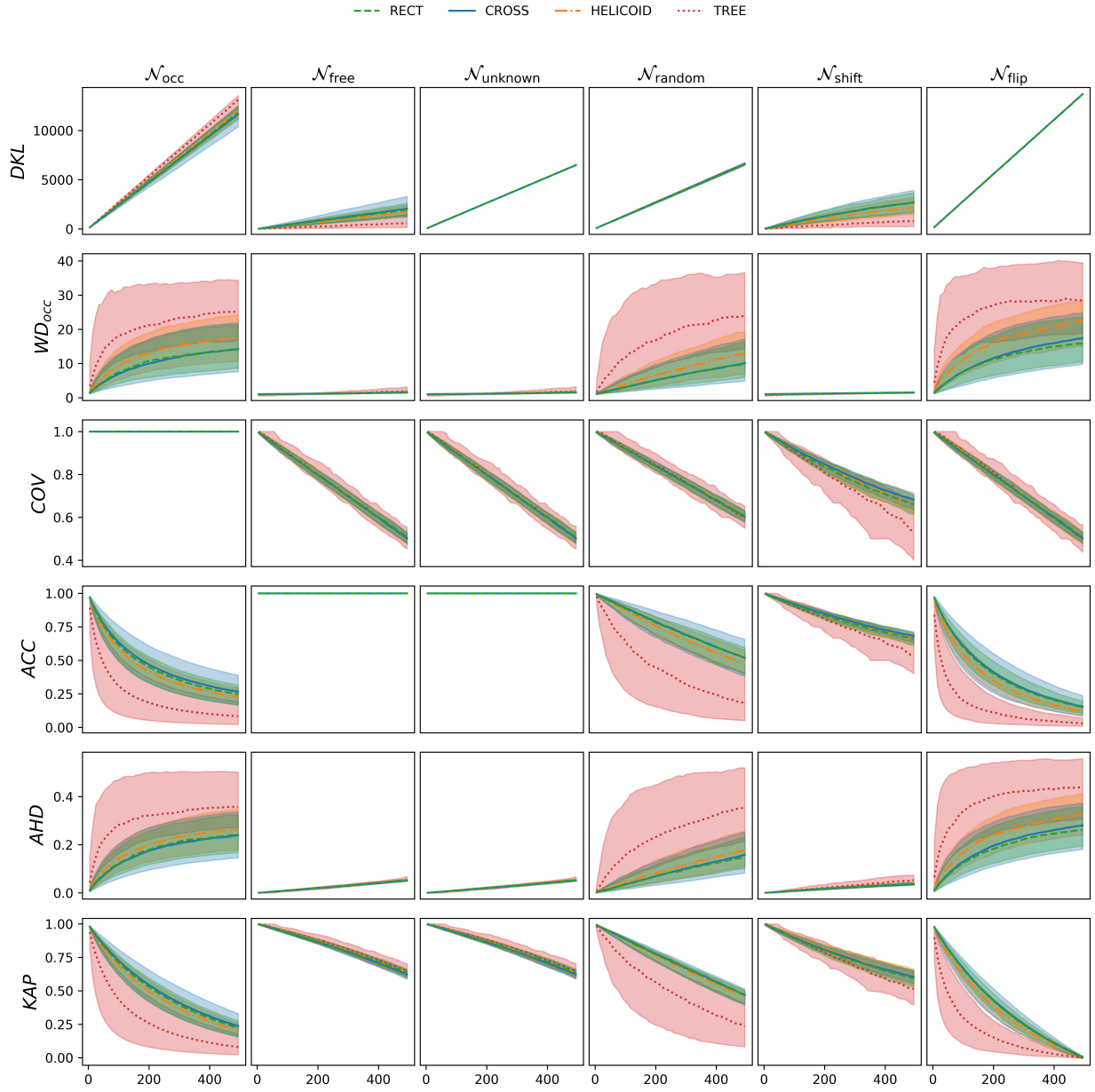


Figure 13: Illustration of the different metrics behavior when the reconstruction moves further from the ground-truth. One line per metric, one column per type of degradation applied to the gt. For each sub-figure, the x-axis is the number of iteration  $n$ , the y-axis the value of the metric  $\theta$ . The results are grouped by type of asset in the world. In each sub-figure, the line corresponds to the median value from all cuboids in the type of world and the filled area shows the spread of 80% of the population.

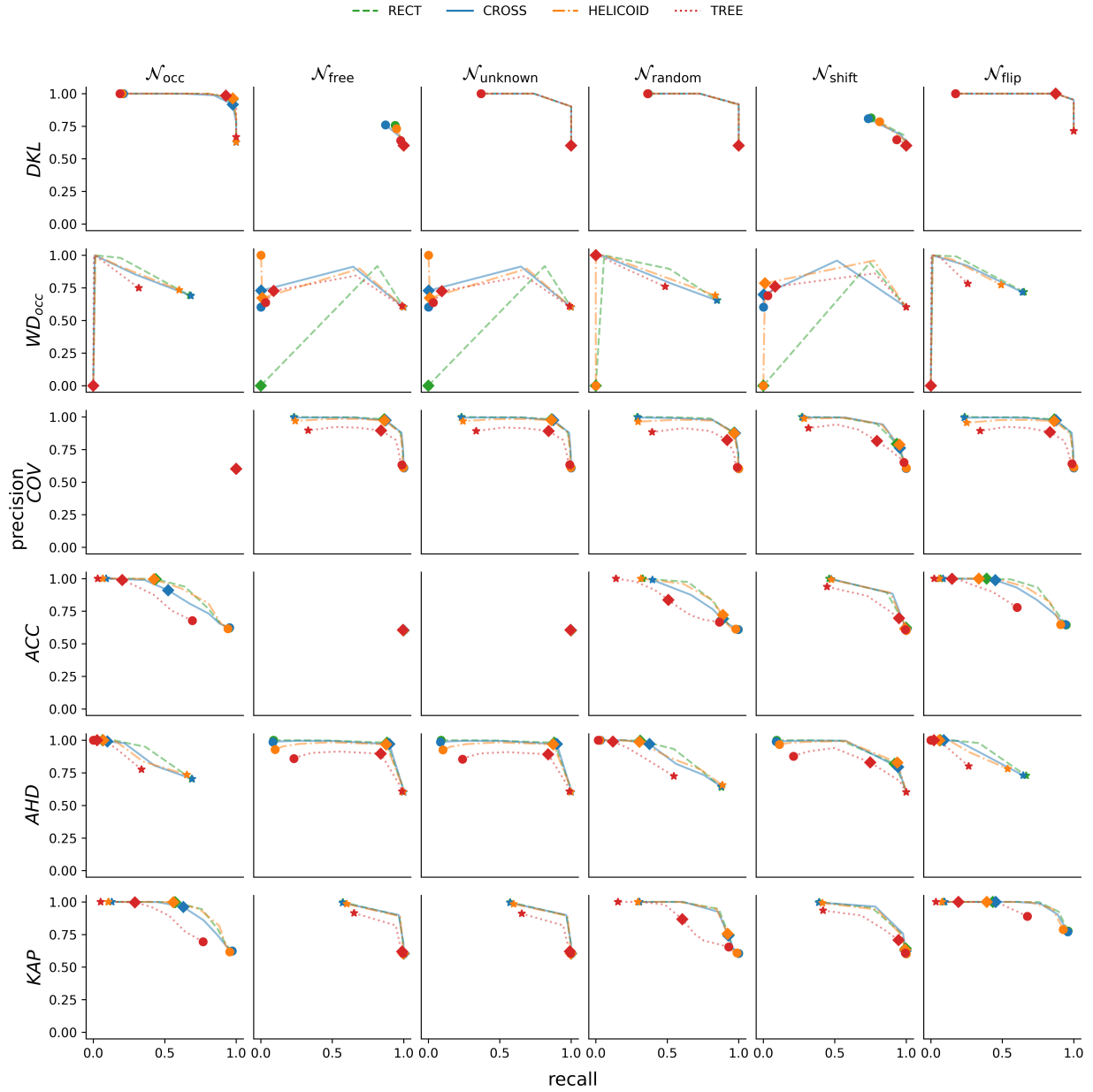


Figure 14: Precision-Recall curves when we vary the value of the threshold  $\hat{\theta}$  for each metric. One line per metric, one column per type of degradation, one color per type of world. The three markers display precision-recall points for three values of  $\hat{\theta}$  for each metric. The results are displayed for a level of degradation of the cuboid of 20%. The points in (0,0) corresponds to points where it is not possible to compute precision and recall (division by 0 in Eq. 13 and 14)